



Singlet oxygen generation potential of porphyrin-sensitized magnetite nanoparticles: Synthesis, characterization and photocatalytic application

M. Neamțu^{a,*}, C. Nădejde^a, V.-D. Hodoroaba^b, R.J. Schneider^b, U. Panne^{b,c}

^a Alexandru Ioan Cuza' University of Iasi, Interdisciplinary Research Department – Field Science, Lascar Catargi Str. 54, 700107 Iasi, Romania

^b Bundesanstalt für Materialforschung und -prüfung (BAM), Unter den Eichen 87, 12205 Berlin, Germany

^c Humboldt-Universität zu Berlin, Department of Chemistry, Brook-Taylor-Str. 2, 12489 Berlin, Germany

ARTICLE INFO

Keywords:

Magnetic Photocatalysts
Porphyrin
Bisphenol A
Photooxidation
Singlet oxygen

ABSTRACT

Singlet oxygen generation potential of two novel free-base-porphyrin photocatalysts was investigated. The free-base-porphyrin-sensitized Fe₃O₄ magnetic nanoparticles (MNPs) were tested for the degradation of the model pollutant Bisphenol A (BPA) in aqueous solution, for the first time. MNPs with either cubic or spherical shape were synthesized using the sonochemical approach, followed by sensitizing with photoactive 4,4',4'',4'''-(Porphine-5,10,15,20-tetrayl)tetrakis(benzoic acid) (TCPP). The resulted photocatalysts were characterized in detail by scanning and transmission electron microscopy, Brunauer–Emmett–Teller analysis, spectral techniques and vibrating sample magnetometry. The electron spin resonance experiments have confirmed the high activity of the photocatalysts through the efficient formation of singlet oxygen in solution. The optimum operational parameters for BPA degradation were established as follows: 1.0 μmol L⁻¹ BPA, 1.0 g L⁻¹ of photocatalyst, 100 μmol L⁻¹ H₂O₂, under UVA irradiation. In these conditions, the results for both photocatalysts revealed that after only 10 min of reaction, over 64% and ca. 90% of BPA have been removed from solution in the absence and presence of H₂O₂, respectively. Whereas after 60 minutes of treatment, only 24% of BPA in real wastewater effluent samples were removed under UVA irradiation in the absence of H₂O₂, showing the high complexity of real wastewater. Moreover, both photocatalysts were successfully used for BPA removal in three consecutive runs, without significant loss of catalytic features.

1. Introduction

Advanced Oxidation Processes (AOPs), such as photocatalysis, have gained a major interest in the field of water remediation as a modern, viable technology for the complete photocatalytic mineralization and removal of a variety of organic pollutants from water [1–5]. Together with the rapid development of photocatalytic oxidation procedures, a high demand has emerged for environment-friendly techniques and suitable catalytic materials required to efficiently perform under various operational conditions. An appealing option for green photocatalysts are the compounds from the porphyrin family. Porphyrins [6] are regarded as valuable photosensitizers, characterized by intense absorption of UV–vis light; their absorption spectra are dominated by strong bands: B (Soret band) in the 350–450 nm region and Q in the 500–700 nm range (resulted from the $\pi-\pi^*$ electronic transitions between HOMO and LUMO energy levels). Besides the high activation in the presence of light due to their large conjugated structure, numerous desirable features recommend porphyrins as attractive options for greener technologies in the photocatalysis field, such as: enhanced

chemical and photostability, high photogenerated ¹O₂ yield, excellent electron donating properties due to their large π -electron systems, ability to undergo photoinduced multielectron transfer without changing their structure, etc. Thus, the studies on natural and synthetic porphyrins and their metallo-derivatives provided the knowledge to successfully develop and apply bioinspired porphyrin-based photocatalysts in various fields of research: light-driven catalysis [7], application in solar-energy conversion [8], photodegradation of a wide range of organic and inorganic pollutants in air and water [9,10], photodynamic therapy [11,12], inactivation and elimination of bacteria [13,14], viruses [15], cancer cells [16], as well as the development of a wide range of sensing materials [17–19].

By immobilizing porphyrin-based catalysts on organic or inorganic solid supports, multifunctional nanometer-scale materials are developed, facilitating their recovery from the reaction medium by applying a magnetic field. Different materials have been employed as immobilization substrate: various types of polymeric matrices [20–23], clays and layered materials [24–26], ion-exchanging resins [27], different types of zeolites [28], modified silica [29,30], microporous

* Corresponding author.

E-mail address: mariana.neamtu@uaic.ro (M. Neamțu).

porphyrin framework solids [31], hydrogels [32], as well as a variety of nanostructures such as iron oxide nanosystems [33–35], TiO₂ nanopowders [36], graphite-like carbon nitride nanosheets [37], nanohybrid films [38], etc.

Various porphyrin-sensitized magnetic photocatalysts have been designed for the photooxidation of various pollutants [23,33,34,39–43]. Among the wide array constituting the porphyrin family, 4,4',4'',4'''-(Porphine-5,10,15,20-tetrayl)tetrakis(benzoic acid) (TCPP) has been highlighted as a highly effective photosensitizer for singlet oxygen generation [44]. Thus, TCPP was selected in the present study as photosensitizer for immobilization on Fe₃O₄ MNPs. Moreover, the anchoring of TCPP onto nano-sized magnetic supports, such as functionalized magnetic nanoparticles (MNPs), allows the easy recovery of the catalyst from the reaction mixture. The new porphyrin-based hybrid system will exhibit enhanced photocatalytic activity, comparable to that of a non-anchored sensitizer [44].

In this work, we report the synthesis, characterization and catalytic activity of TCPP-PEG functionalized MNPs. The proposed photocatalysts were tested in the degradation of Bisphenol A (BPA), a non-biodegradable and hazardous compound, commonly used as a test model; their catalytic performance was investigated in either pure aqueous solution or complex matrices such as influent and effluent samples from WWTP. The generation of singlet oxygen by nanocatalysts after three consecutive runs has also been proven.

2. Experimental

2.1. Materials

High purity chemicals (Sigma-Aldrich) were used as purchased in all experiments. The photoactive free-base porphyrin 4,4',4'',4'''-(Porphine-5,10,15,20-tetrayl)-tetrakis-(benzoic acid), dye content 75% (TCPP) was chosen as sensitizer. Fresh ultrapure water (0.055 µS cm⁻¹) obtained from a water purification system (LaboStar™ Pro TWF UV, Evoqua) was used throughout all experimental procedures. The photocatalyst activity was also tested on two types of wastewater samples (influent and effluent), collected from a Municipal Wastewater Treatment Plant (WWTP) in Berlin, Germany, which treats both household and industrial sewage (purification capacity of 240,000 m³/day). More details, together with the measured basic parameters of WWTP samples, are given in Table S1 (see SI file).

2.2. Photocatalyst preparation

Two porphyrin-sensitized photocatalytic magnetic materials were obtained in the present study, which differ in their magnetite (Fe₃O₄) core morphology (either cubic or spherical-shaped nanoparticles). The first step in photocatalyst preparation was the sonochemical synthesis of different-shaped magnetite nanoparticles (MNPs). Sonochemistry proved to be a powerful tool to produce MNPs with tunable improved properties (various shapes, more uniform size distribution, higher specific surface area, etc.) compared to the classical co-precipitation method using magnetic/mechanical stirring. The ultrasound assistance ensures a more uniform and faster reaction; moreover, the shock waves significantly increase the hydrolysis rate and determine morphological changes in the resulting particles [45–47]. The detailed procedures describing the synthesis of two types of MNPs, with cubic (C1) or spherical (C2) morphology, can be found in SI. The as-synthesized two types of MNPs were subsequently stabilized with polyethylene glycol (PEG) (average M_{wPEG} = 3,350, Polydispersity Index 1.05–1.10) in order to prevent nanoparticle oxidation and agglomeration. PEG coating also serves as an excellent ligand for the immobilization of the photosensitizer (TCPP) on the nanomaterial surface, in the final preparation stage. For MNPs stabilization, PEG (2 mol L⁻¹) was added dropwise to the Fe₃O₄ sludge, and kept under vigorous mechanical stirring for 1 h at 60 °C. The products were purified by alternating

magnetic decantation with rinsing, using pure water and absolute ethanol, and then used for further immobilization of TCPP. The TCPP solution (5 mmol L⁻¹, pH 8.0) was gradually added to the PEG coated MNPs under mechanical stirring for 30 minutes at 50 °C. The resulted suspensions (Fe₃O₄/PEG/TCPP) were then ultrasonically dispersed for another 60 minutes at constant temperature (50 °C). The materials were again washed through repeated magnetic decantation and rinsing with pure water. Then, after subsequent drying in a vacuumed oven at 50 °C, the two photocatalysts, C1 (corresponding to the cubic-shaped Fe₃O₄/PEG/TCPP nanostructures) and C2 (spherical Fe₃O₄/PEG/TCPP nanoparticles), were ready to be tested.

2.3. Characterization of photocatalysts

The resulted photocatalysts, C1 and C2 were characterized in detail. The morphological analysis of the particulate materials has been carried out with an SEM (scanning electron microscope) of type Zeiss Supra 40 (Oberkochen, Germany) with a Schottky field emitter and equipped with a high-resolution *In-lens* SE (secondary electrons) detector. Elemental analysis has been performed with an EDS detector of type SDD (silicon drift detector) from Bruker Nano GmbH (Berlin, Germany). High resolution transmission electron microscopy (HR-TEM) (Zeiss Libra 200 MC TEM/STEM electron microscope) was used in order to get a detailed view of the morphology of the samples.

The photocatalyst surface properties were assessed by N₂ adsorption-desorption isotherms using the Brunauer–Emmett–Teller (BET) method. The measurements were carried out at 77 K and relative pressure (P/P_0): 0–0.99, on a Micromeritics ASAP 2020™ Physisorption system (Norcross, USA); the Barrett–Joyner–Halenda (BJH) method was also employed to calculate the mean diameter and volume of the sample pores. All samples were degassed under vacuum at 105 °C for 4 h before the N₂ isotherms recordings.

The crystalline structure of both photocatalysts was analyzed by a Bruker AXS D8 ADVANCE diffractometer (Bragg-Brentano configuration, θ - θ geometry, characteristic Cu K α radiation (λ = 0.15418 nm), 40 kV, 40 mA, range of 2θ = 20– 80°, speed: 2 s/step; scanning step 0.02°). The DIFFRAC^{plus} Eva software was used for data analysis together with Scherrer's formula for the estimation of the mean crystallite size.

Fourier transform infrared (FTIR) spectra of the powdered photocatalysts and their constituents, prepared in KBr discs, were recorded on a Jasco 6100 spectrometer (4000–400 cm⁻¹ range, 4 cm⁻¹ resolution) at room temperature.

The magnetization curves of the prepared photocatalysts were obtained on a Lake Shore 7410 vibrating sample magnetometer (VSM) at room temperature.

The detection of the ¹O₂ generated in solution in the presence of the photocatalysts was carried out through electron spin resonance (ESR) spectroscopy in order to confirm the activity of the photocatalysts. An ESR Spectrometer device (MiniScope MS 300, Magnettech GmbH, Berlin, Germany) was used at a microwave power of 0.1 mW. The typical instrumental settings were: B₀-field 336 mT, sweep width 10 mT, sweep time = 60 s, and a modulation amplitude of 0.2 mT. Samples of 5 mL volume of pollutant aqueous suspensions at the room temperature containing the photocatalyst and 40 mmol L⁻¹ of 2,2,6,6-tetramethyl-4-piperidinol (TMP-OH) were exposed to UVA (λ = 365 nm, from a Lightingcure™ UV spot light source, model LC-8, from Hamamatsu Photonics, Germany; photon flow: 9.11×10^{-8} Einstein s⁻¹, irradiation depth: 1.2 cm, irradiated surface: 5.72 cm²). During illumination, the suspensions were equilibrated with oxygen at atmospheric pressure. In order to record the ESR traces, 50 µL aliquots of illuminated suspensions were transferred into glass capillary tubes (0.7 mm ID, 0.87 mm OD, sample height of about 40 mm) and sealed on both ends with Cha-seal (Chase Scientific Glass, Rockwood, TN, USA). Furthermore, they were placed into quartz glass tubes (inner diameter of 4 mm, Magnettech GmbH, Berlin, Germany). Continuous wave X-

band ESR-Spectra of TEMPOL, formed from TMP-OH, were acquired at room temperature.

2.4. Catalytic BPA oxidation experiments

The kinetic experiments were performed in mild conditions (initial pH 6.6, ambient temperature $25 \pm 2^\circ\text{C}$) at laboratory scale. The initial concentration of BPA in all experiments was $1.0 \mu\text{mol L}^{-1}$. The reaction was initiated after reaching equilibrium in solution. Furthermore, the solution was analyzed after stabilization occurred, in order to confirm that no adsorption process took place at the photocatalyst surface. The total reaction volume was 5 mL in all experiments; the irradiated surface area was 9.62 cm^2 and the irradiation pathlength 0.8 cm. The photochemical tests using UVA irradiation of the aqueous samples were performed in a Heidolph Titramax 100 orbital shaker equipped with an UVA lamp (three parallel Xe lamps, $290 \leq \lambda \leq 400 \text{ nm}$, 40 W m^{-2} , photon flow of $7.81 \times 10^{-8} \text{ Einstein s}^{-1}$, measured by polychromatic actinometry with phenylglyoxylic acid in $\text{AcN:H}_2\text{O} = 3:1(\text{v/v})$, ATLAS Material Testing Solution, Germany); more details are provided in our previous publications [48,49]. To study the effect of photocatalyst concentration, 0.5, 1.0 and 1.5 g L^{-1} of photocatalyst were evaluated in the BPA degradation experiments at various time intervals with total contact time of 60 min. From a 30% H_2O_2 standard solution, three concentrations of 100, 150 and $200 \mu\text{mol L}^{-1}$ were used to evaluate the catalytic behavior. During kinetic experiments, aliquots from each sample were withdrawn regularly, immediately filtered ($0.22 \mu\text{m}$ Teflon membrane) and submitted for HPLC analysis (HPLC–MS/MS system) in order to measure the BPA concentration in each tested sample. An 1100 HPLC workstation (Agilent Technologies, Waldbronn, Germany) was used for analyses, coupled to an API 6500 TSQ triple stage quadrupole mass spectrometer (ABSciex, Darmstadt, Germany). The detailed description of the experimental set-up and method of analysis can be found in our previous study [48].

3. Results and discussion

3.1. Photocatalyst characterization

The morphology of the freshly prepared photocatalysts was assessed by using SEM and TEM (see Fig. 1). Inspecting the morphology of the two samples through high-resolution SEM revealed that the constituent particles have dimensions well below 100 nm and a compact shape, either predominantly cubic in the case of C1 (Fig. 1a) or spheroidal for the C2 photocatalyst (see Fig. 1d). At a closer observation of the high-resolution SEM micrographs in Fig. 1, the sharp edges of the nanoparticles suggest their crystalline structure. The size of the nanoparticles constituting sample C1 is about 25–30 nm, in agreement with Dang et al. [46], whilst the particles in sample C2 are smaller, i.e. of about 10 nm and less.

The TEM images (Fig. 1b,c,e,f) emphasize the different morphology of the two types of nanosized magnetic particles: cubic shape - C1 (Fig. 1b,c and Fig. S1a,b (please see SI file)) versus spherical shape - C2 (Fig. 1e,f and Fig. S1c,d (please see SI file)), corresponding to photocatalyst sizes of maximum 34 nm in the case of C1 and up to 15 nm for C2. Thus, the TEM measurements are in agreement with the SEM data. A more detailed morphology was provided by the HR-TEM images (Fig. 1 c,f), which revealed the thin outer TCPP layer of about 1.0–1.5 nm uniformly surrounding the magnetic cores.

The elemental composition of the two samples C1 and C2, as well as of $\text{Fe}_3\text{O}_4/\text{PEG}$ sample (please see Fig. S2 in SI file) has been analyzed by EDX. Due to the strong morphology of the two nano-particulate materials, only a qualitative analysis can be carried out. The presence of C, O and Fe as major elements has been confirmed by representative EDX spectra (see Fig. 2).

After normalization to the intensity of O K X-ray peak, the comparison between the atomic fractions of C1 and C2 is possible and a

significantly larger amount of C in sample C2 becomes evident. Note the weak presence of nitrogen (see inset in Fig. 2) in both samples (somewhat more in C2) as an indicator for the porphyrin layer surrounding the MNPs. The slightly higher fraction of N in C2 (see inset in Fig. 2) together with the significantly higher intensity of C K in the EDX spectrum indicate that the porphyrin (containing both C and N), designed as shell of the magnetite nanoparticles, is present in C2 to a larger extent (as thicker shell) than in C1.

The powder XRD patterns of C1 and C2 samples revealed that magnetite was the dominant crystalline phase with sharp diffraction peaks in both samples, characterized by the typical cubic inverse spinel structure of iron oxide nanoparticles (Fig. 3a). The characteristic peaks of magnetite were identified at 2θ values of ca. $30.2, 35.6, 43.3, 53.7, 57.2$ and 62.8° , corresponding to (hkl) Miller indices of (220), (311), (400), (422), (511) and (440), respectively. The data is consistent with the Fe_3O_4 reference pattern (JCPDS card no. 00-019-0629). The average crystallite size of each type of MNPs was estimated from the full width at half-maximum of (311) plane in the XRD patterns, using the Debye-Scherrer equation, the values being presented in Fig. 3a. The narrower sharp diffraction peaks of C1's XRD pattern compared to the broader ones of C2 confirm that C1 possesses grains of increased crystallite sizes in comparison with C2, the findings being consistent with the SEM and TEM results (Fig. 1).

The N_2 adsorption-desorption isotherms (Fig. 3b) were recorded in order to assess the surface properties of both photocatalysts. The narrow hysteresis loops characterizing the isotherms were identified to be of type IV (IUPAC classification). The two materials possess different surface properties due to their morphology and size of the constituent nanoparticles (cubic C1 vs. spherical C2, Table 1): the results show a larger specific surface area for C2 compared to that of C1, pointing at constituent particles of smaller size, in agreement with the SEM, TEM and XRD results; thus, C2 offers a larger inner area than C1 for the potential formation of porphyrin shell onto the constituent MNPs. Furthermore, C1's average pore size is more than double the value of C2, consistent with the different morphology and size of the constituent particles found with SEM and TEM, i.e. the smaller, spheroidal C2 NPs are packed together tighter than the larger, cubical-like C1 NPs arranged irregularly to each other. This interplay of morphology, size and spatial arrangement of the two types of constituent MNPs of C1 and C2 finally leads to a similar pore volume.

The FTIR measurements offered information regarding the bonding characteristics for each photocatalyst (Fig. 3c). Both photocatalysts exhibit the specific strong vibration band of Fe–O in the lower wave-number region (around 580 cm^{-1}) given by Fe stretching at the tetrahedral site in magnetite [34,35]. The presence of TCPP on the MNPs surface was confirmed by FTIR measurements, in agreement with the elemental EDX analysis. The specific bands of TCPP are present in both photocatalysts with vibration peaks of lower intensity than the ones in the pure TCPP, suggesting the linking of porphyrin on the MNPs surface. The peaks around 784 and 970 cm^{-1} are assigned to the N–H out-of-plane vibrations and to the in-plane stretching in TCPP, respectively, while the peak at 1110 cm^{-1} is given by the vibration of the opposite pyrrole rings. The C–H stretching vibration of TCPP was identified at 1255.75 cm^{-1} . The peaks at ca. 1690 and 1600 cm^{-1} are associated with the vibrations of C=C and C=N groups of TCPP, while the signal at 1700 cm^{-1} is assigned to the carbonyl group (C=O) of the carboxyl acid in TCPP [34]. The broad peaks around 2500 and 3000 cm^{-1} correspond to the aromatic and aliphatic C–C stretches in TCPP [35]. The broadened peak in the $3300\text{--}3450 \text{ cm}^{-1}$ range is ascribed to the O–H signal of the carboxyl group overlapping the peak associated with the N–H stretching vibration, both being present in both photocatalysts, as well as in the spectrum of TCPP [34]. The results demonstrate that TCPP was successfully immobilized on the MNPs surface.

The photocatalysts magnetic properties were evaluated by VSM measurements at room temperature (Fig. 3d). The obtained magnetic photocatalysts exhibit good magnetic properties, with similar high

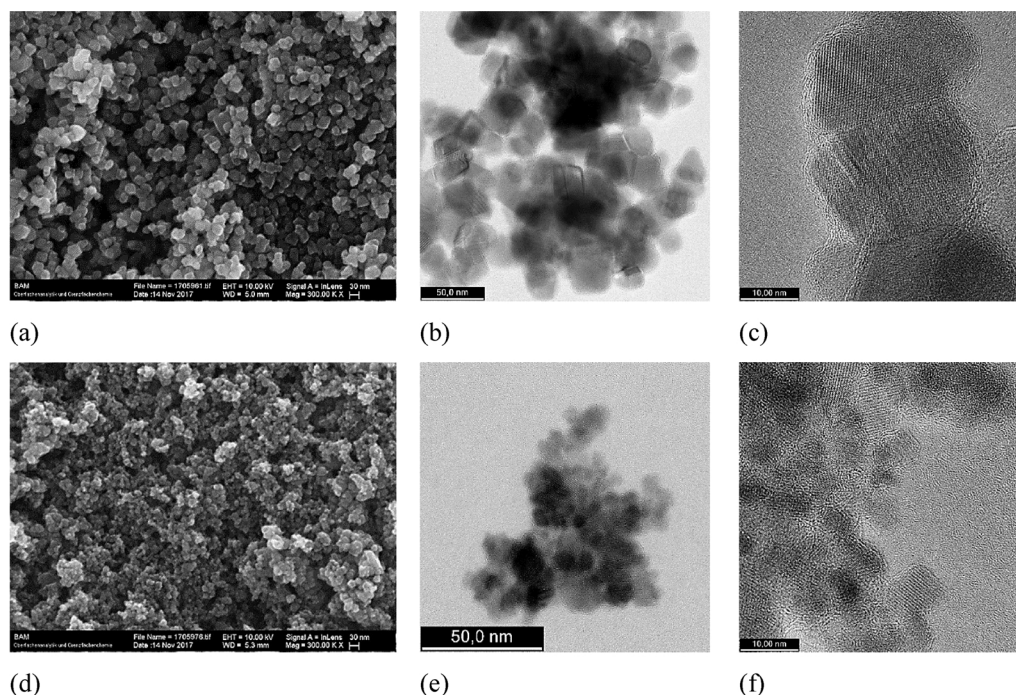


Fig. 1. Sample C1:(a) SEM micrograph; (b) TEM and (c) HR-TEM images of C1 photocatalyst; Sample C2: (d) SEM micrograph; (e) TEM and (f) HR-TEM images of C2 photocatalyst.

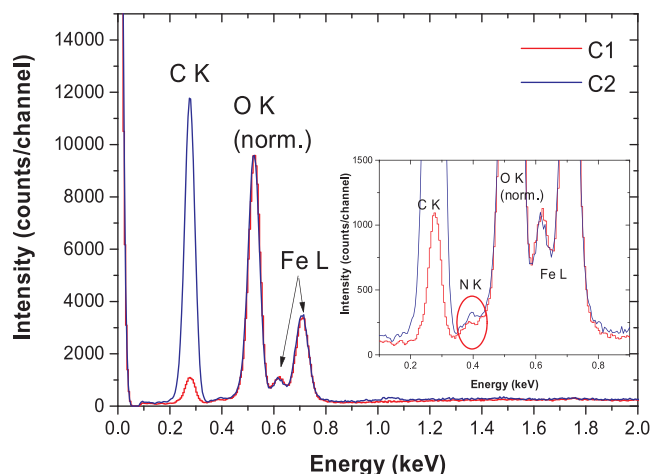


Fig. 2. 15 kV EDX spectra of the two samples C1 and C2 (summed over an area of about $50\ \mu\text{m} \times 50\ \mu\text{m}$) normalized to the height of O K peak intensity.

saturation magnetization values of $48.35\ \text{A m}^2\ \text{Kg}^{-1}$ for C1 and $51.18\ \text{A m}^2\ \text{Kg}^{-1}$, respectively, for C2 (Fig. 3d). As expected, the decreased values of saturation magnetization of C1 and C2 submicron particles compared to the one of bare MNPs ($69.36\ \text{A m}^2\ \text{Kg}^{-1}$) [48] are attributed to the presence of the organic shells surrounding the magnetic cores. The good magnetic features allow facile extraction of the photocatalysts from solution using an external magnet and their reuse in consecutive runs of water decontamination. The results are in agreement with scientific reported data [50].

ESR method was applied for the detection and identification of the active species generated by TCPP immobilized on MNPs in reaction. It has been established that porphyrins can be excited under photo-irradiation, triggering the generation of singlet oxygen ($^1\text{O}_2$) [51,52]. The singlet oxygen yield, generated by the photocatalysts in solution under UVA irradiation was measured by ESR (Fig. 4, Table 2).

The diamagnetic scavenger 2,2,6,6-tetramethyl-4-piperidinol (TMP-OH) was used as spin trap, since it reacts with $^1\text{O}_2$, yielding a stable

paramagnetic product, 4-hydroxy-2,2,6,6-tetramethylpiperidine-1-oxyl (TEMPO) that can be easily detected by ESR. The spectral parameters $\Delta H_{pp} = 1.58\ \text{G}$, $g = 2.00570$, and $\alpha_N = 17.13\ \text{G}$, are typical for TEMPO [48]. The reactive scavenging of $^1\text{O}_2$ by TMP-OH is considered to be highly specific for $^1\text{O}_2$. The ESR results have confirmed the photocatalysts' high activity through the efficient formation of high amount of singlet oxygen in solution (Table 2).

As depicted in Fig. 4, the ESR spectra consist of three equidistant and equi-intense hyperfine lines in each ESR spectrum. Figs. 4a and b shows how the signal peaks gradually increase with the increase of irradiation time – this indicating that $^1\text{O}_2$ is increasingly formed in time. Our results are in agreement with those reported by different authors for other porphyrin-based catalysts [23,51,53].

3.2. Photocatalytic activity

The BPA degradation experiments were conducted in order to establish the optimum operational parameters for pollutant removal, such as catalyst dosage, H_2O_2 concentration and contact time. The photocatalytic activities of the two studied photosensitized catalysts were evaluated for the photodegradation of BPA in different types of water (Fig. 5).

The photooxidation experiments were carried out using a BPA initial concentration of $1.0\ \mu\text{mol L}^{-1}$, at near-neutral initial pH, at room temperature, under UVA irradiation, in absence and in presence of H_2O_2 , respectively. The reactions were initiated after reaching the adsorption/desorption equilibrium between photocatalyst and pollutant.

Under UVA exposure, both photocatalysts exhibited similar photocatalytic activities, which increase with contact time. Initially, the reaction increased when enhancing the material dosage from 0.5 to $1.0\ \text{g L}^{-1}$, however, by subsequent increase of photocatalyst amount to $1.5\ \text{g L}^{-1}$, no significant additional photodegradation of BPA was noticed for any of the two photocatalysts. Around 82% of BPA degradation was achieved after 60 min of reaction (Fig. 5a) by using $1.0\ \text{g L}^{-1}$ of photocatalysts. Thus, in the presence of UV light, the degradation of BPA is rapid and efficient due to the direct oxidation by $^1\text{O}_2$. By testing among the three different dosages, an optimal concentration of

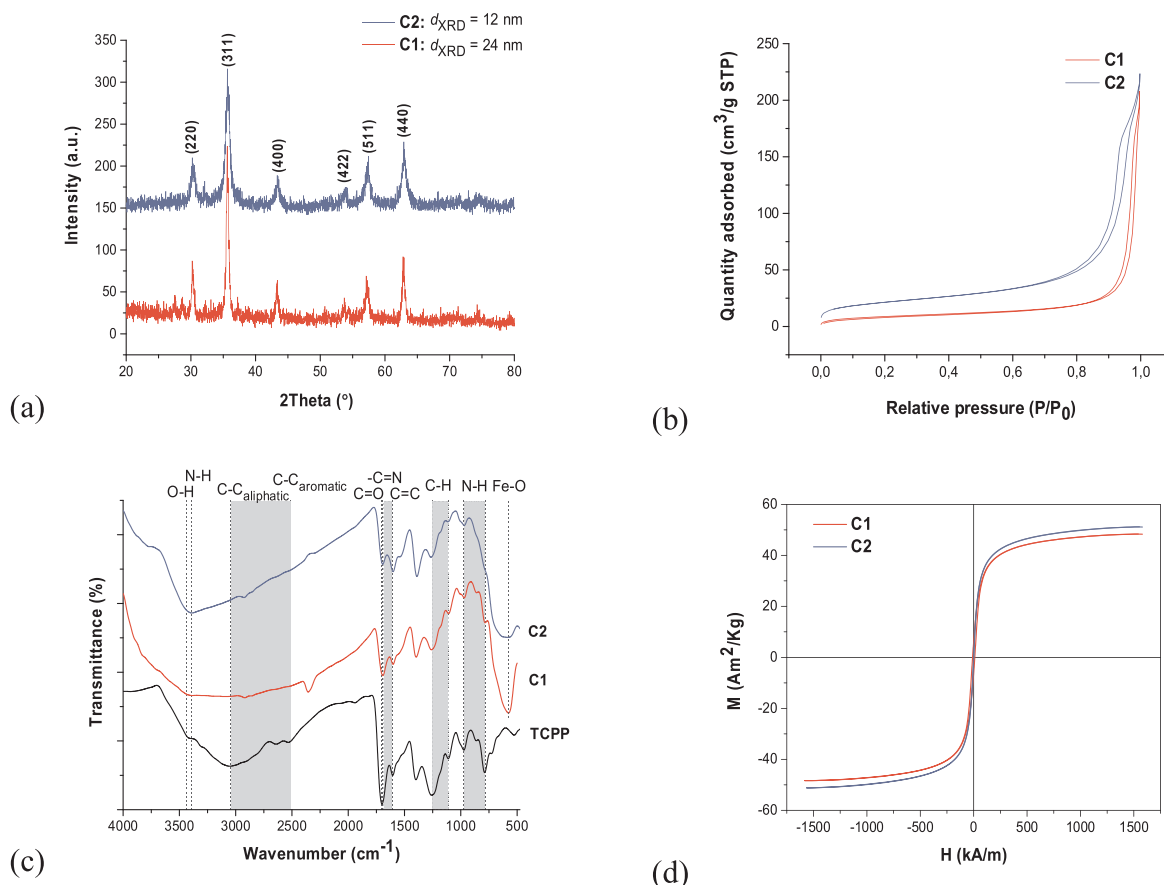


Fig. 3. (a) XRD patterns of the studied photocatalysts, C1 (cubic) and C2 (spherical), and the corresponding average crystallite size of the Fe_3O_4 nanoparticles (Scherrer equation); (b) The nitrogen adsorption-desorption isotherms and pore size distribution curves (inset) of the two photocatalysts; (c) FTIR spectra of the magnetic photocatalysts and pure TCP; (d) The room temperature magnetic hysteresis loops of the photocatalysts.

Table 1

Results of BET method and SEM analysis performed for the synthesized photocatalysts.

Photocatalyst type	SEM particle size (nm)	BET surface area ($\text{m}^2 \text{g}^{-1}$)	BJH pore size (nm)	Pore volume ($\text{cm}^3 \text{g}^{-1}$)
C1 (cubic)	25–30	32.38	39.66	0.32
C2 (spherical)	≤ 10	77.19	17.91	0.35

1.0 g L^{-1} of photocatalyst gave the best results for both materials (see Fig. 5a), which was selected for further use in the following kinetic degradation tests.

High catalytic behaviors were reported by numerous authors when testing different types of porphyrins-based photocatalysts. The photo-oxidation of phenol and monochlorophenols by irradiation with visible light in aqueous alkaline solution in the presence of TCP and oxygen has been described by Gerdes et al. [54]. Fernandez et al. [42] evaluated the photocatalytic activity of various types of porphyrin anchored onto Fe_3O_4 MNPs in the degradation of 17 β -estradiol (E2) assisted by visible light irradiation. In the presence of $10 \mu\text{mol L}^{-1}$ of porphyrin-based on Fe_3O_4 nanoparticles it was possible to remove ca. 82% of the initial E2 after 8 h of irradiation. The high photocatalytic performance of porphyrins encapsulated onto different supports such as TiO_2 , SiO_2 , nanofibers or porous materials in the degradation of rhodamine B, phenol, 4NP, 4chlorophenol (4CP), 2,4dichlorophenol (2,4 DCP) or 2,4,6trichlorophenol (2,4,6TCP) as model pollutants, validate their use as hybrid photocatalysts for the degradation of persistent pollutants in water treatment [7,43,53,55]. Other porphyrin-based photocatalysts were reported for highly efficient degradation of a wide range of toxins,

hazardous microrganisms or cancer cells, mainly involving the effect of photosensitized singlet oxygen production and electron transfer. Fakayode et al. [23] highlighted the very high singlet oxygen generation potential of an iron oxide–gold core-shell PEGylated porphyrin conjugate both in UV and visible domain, intended for photodynamic therapy. On the other hand, Yoo et al. [30] demonstrated the efficacy of tin porphyrin immobilized on silica substrate able to accelerate the degradation of Microcystin (MC) toxins under visible light irradiation, reducing the concentration of toxin in the reaction medium to an undetectable level after 40 minutes; a photo-initiated electron transfer from MC to the triplet state of the catalyst was identified at the main degradation rate of about 95% after 6 hours under visible light irradiation in mild conditions using a recyclable magnetic catalyst based on hemin with axial ligand ($[\text{BPA}]_0 = 20 \text{ mg L}^{-1}$; $[\text{catalyst}] = 0.15 \text{ g L}^{-1}$).

The photosensitizer plays a key role: TCP possesses a high photochemical electron-transfer ability and it is an important source of singlet molecular oxygen ($^1\text{O}_2$), generated under light exposure. The generation of $^1\text{O}_2$ is usually the proposed mechanism responsible for pollutant break-down and its removal from aqueous medium in the process of photodegradation over light-activated TCP. Following the excitation of the photosensitizer, the absorbed light promotes the energy transition from the ground state (S_0) to the singlet-excited state of the photocatalyst (S_1^*), then undergoes intersystem crossing to the triplet-excited state (T_1^*) which has longer lifetime than S_1^* ; this enables the photosensitizer to react through one of the two photochemical mechanisms: Type I or Type II. The Type I mechanism refers to the electron-transfer between the activated porphyrin and a substrate, generating free radicals. The Type II mechanisms involves the $^1\text{O}_2$ yield

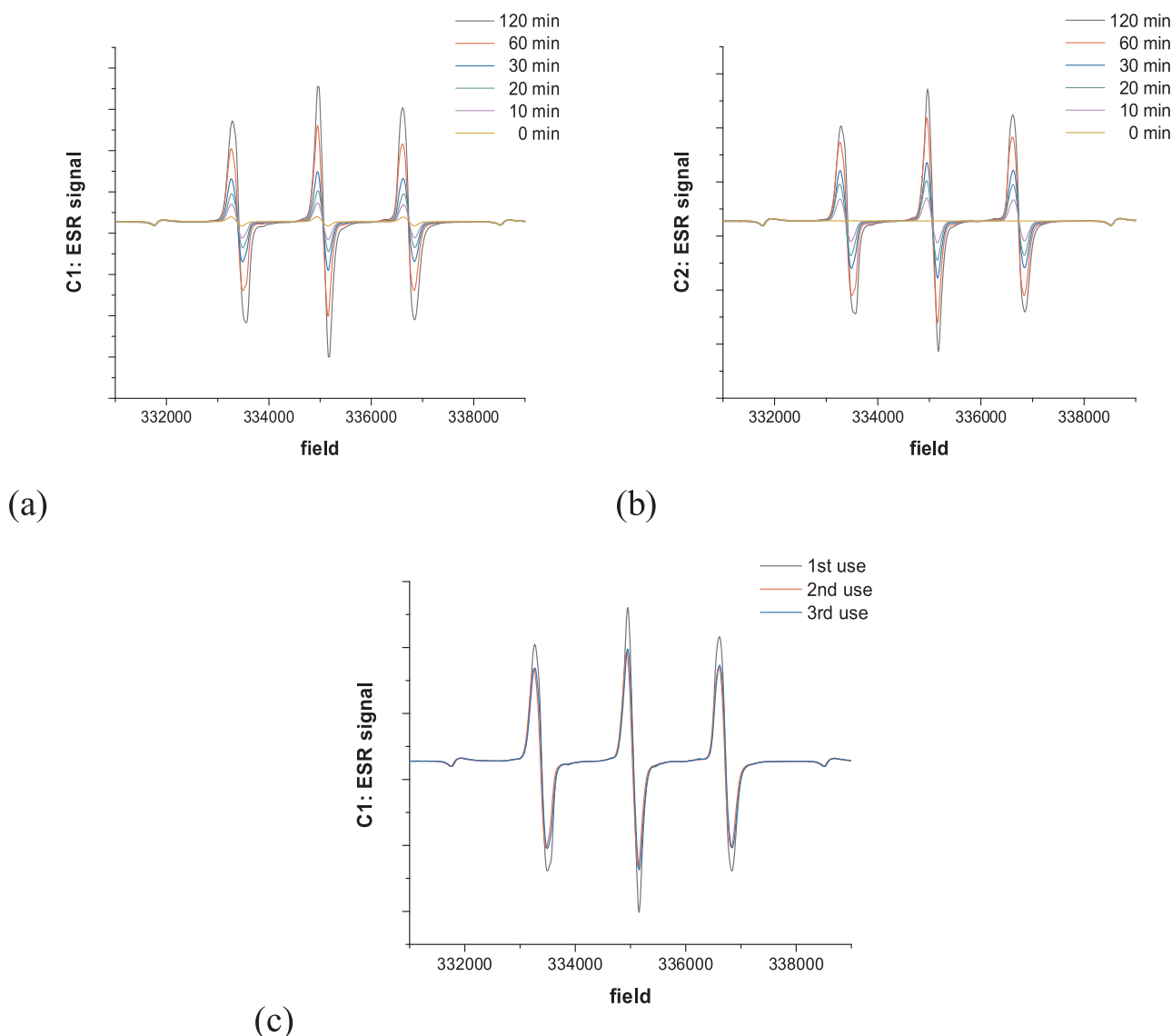


Fig. 4. ESR signals of TEMPOL under UVA irradiation ($\lambda = 365$ nm) in the presence of (a) C1 photocatalyst; (b) C2 photocatalyst; (c) three consecutive runs of C1 photocatalyst. Initial conditions: 1.0 g L^{-1} photocatalyst, 40 mmol L^{-1} of TMP-OH, photon flow of $9.11 \times 10^{-8} \text{ Einstein s}^{-1}$, irradiation depth of 1.2 cm, irradiated surface of 5.72 cm^2 , room temperature.

Table 2

Concentration of $^1\text{O}_2$ ($\mu\text{mol L}^{-1}$) generated by TCCP-PEG functionalized MNPs.

Time (min)	C1			C2
	1st use	2nd use	3rd use	1st use
0	0.00	0.00	0.00	0.00
10	90.27	42.11	36.84	85.08
20	149.27	97.45	85.42	149.74
30	238.72	152.12	124.00	214.06
60	446.85	309.07	334.96	368.03

during an energy transfer process triggered by the collision of the excited porphyrin, T_1^* and triplet oxygen [43,44]. Fe_3O_4 cores, which provide the magnetic function of the material, can also contribute in the generation of electrons and holes in the valence band. Meng et al. [53] confirmed that $^1\text{O}_2$ generated from porphyrin ligand within catalytic system under visible light was directly responsible for highly efficient BPA oxidation; they further suggested that the lack of the hydroxylated products in reaction is an indication that the process is not based on any other free radicals than $^1\text{O}_2$ alone [53].

The BPA decomposition can be accelerated even more by adding an oxidizing agent in solution, i.e. H_2O_2 (Fig. 5b). The reactions among the generated reactive oxygen species (ROS, i.e. hydroxyl radicals) trigger the degradation of BPA at a higher rate. Once the optimal photocatalyst dosage has been established, we have further explored the catalytic performance of the materials in the presence of hydrogen peroxide. The best results were obtained in the presence of $100 \mu\text{mol L}^{-1} \text{H}_2\text{O}_2$; the results revealed that after only 10 minutes of reaction, both photocatalysts have degraded ca. 90% of BPA in pure aqueous solution. No significant improvement of pollutant removal was obtained by further increasing the oxidant dosage beyond $100 \mu\text{mol L}^{-1} \text{H}_2\text{O}_2$, since the excess H_2O_2 in solution may cause the consumption of the generated ROS (i.e. hydroxyl radicals) and slow down the reaction [56]. Note also that no significant degradation of BPA occurred in the presence of H_2O_2 alone (in the absence of the photocatalysts) under light irradiation (Fig. 5b). High catalytic removal of BPA (80.3%) from aqueous solution was also achieved by Tang et al. [40] in the presence of hemoglobin immobilized on amino-modified MNPs, H_2O_2 , pH 7, at 35°C . Therefore, the optimum operational parameters were established as follows: 1.0 g L^{-1} of photocatalyst, $100 \mu\text{mol L}^{-1} \text{H}_2\text{O}_2$, under UVA irradiation,

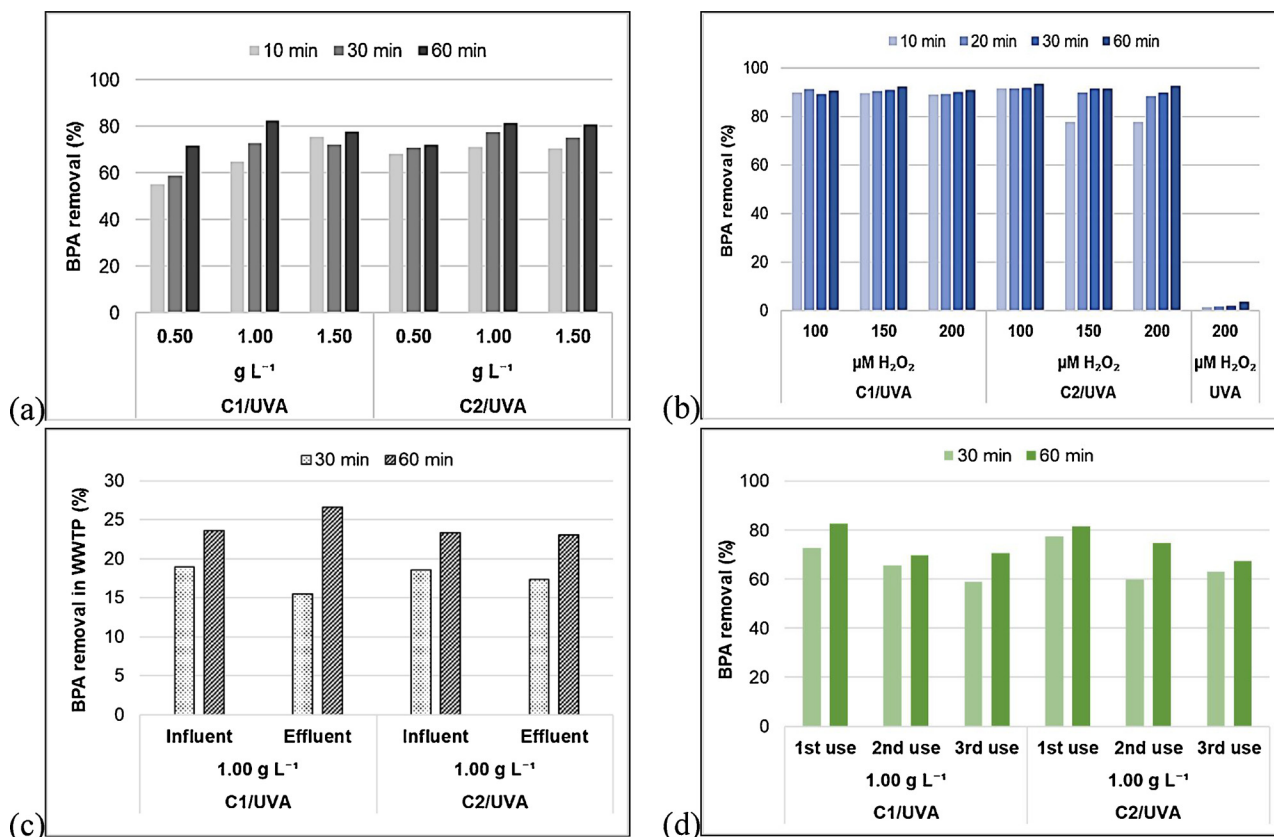


Fig. 5. (a) Effect of photocatalyst concentration; (b) Catalytic performance of the photocatalysts in the presence of H₂O₂; (c) Photocatalyst activity in real WWTP water samples; (d) Reusability experiments. Initial conditions: 1.0 μmol L⁻¹ BPA, 1.0 g L⁻¹ of photocatalyst, UVA irradiation, pH 6.6, *T* = 25 °C; (c) and (d) in absence of H₂O₂.

proving that the photocatalyst, the light exposure and low amount of oxidant are essential for efficient decomposition of BPA in water. However, the BPA removal was low in influents and effluent samples (24%) after 60 minutes of reaction in the absence of H₂O₂ (Fig. 5c), revealing the high complexity of real wastewaters.

In the present study, the detection and identification of intermediates were not performed. BPA degradation products have been extensively reported in literature and in our previous studies [40,53,57–60]. Among others, Meng et al. [53] have detected only 1,4-benzoquinone as a by-product following rapid decomposition of BPA, transformed finally into CO₂ and H₂O, when using TCPP-based photocatalysts. Tang et al. [40] suggest that there could be certain differences in the degradation pathway of BPA when reacting with porphyrin-based photocatalysts, depending on the type of the sensitizer, ranging from native enzymes (horseradish peroxidase) to mimetic ones (free-base porphyrins, metalloporphyrins and their derivatives); they propose that a biodegradation concomitant with a C–C bond cleavage occurs in the process of BPA conversion in the presence of haemoglobin-based catalysts. Nonetheless, the intermediates (which include 1,4-benzoquinone, p-hydroquinone, phenol, 4-isopropylphenol, 4-(1-hydroxy-1-methyl-ethyl)-phenol, etc.) are biodegradable compounds and are further transformed into short-chain aliphatic compounds, and finally, into H₂O and CO₂.

The stability and the recycling capability of the two studied photocatalysts were also evaluated in the present work. The immobilization of TCPP on MNPs provides the possibility of catalyst recovery and reuse while minimizing the environmental impact. After each test was complete, the photocatalysts were recovered from the reaction medium using a magnet, followed by rinsing with pure water and absolute ethanol, and dried in vacuum. Both photocatalysts were successfully used for BPA removal in three consecutive runs without significant loss

of catalytic features (Fig. 5d): about 70% BPA removal was maintained during the reuse cycles; the tests were carried out based on the established optimum operational parameters - 1.0 g L⁻¹ of photocatalyst, under UVA irradiation, in the absence of H₂O₂. Furthermore, it can be seen in Fig. 4d and Table 2, that during photocatalyst reuse, the concentration of ¹O₂ generated by TCPP-PEG functionalized MNPs remains high, thus confirming the high activity of photocatalysts after three consecutive runs. Our previous studies [49,48] showed that the properties of such photocatalysts do not change after consecutive use for pollutant degradation. To our knowledge, the generation of singlet oxygen after three consecutive runs is confirmed by the ESR measurements for the first time. The similar catalytic behavior of both studied nanomaterials, C1 and C2, suggests that the photosensitizer immobilized on the surface of MNPs plays the major role in pollutant degradation.

4. Conclusions

In summary, we have synthesized multifunctional porphyrin-sensitized cubic or spherical MNPs by using facile sono-chemical synthesis procedures. The obtained recyclable photocatalysts showed enhanced catalytic behavior toward the photodegradation of BPA, due to a high yield of singlet molecular oxygen generated by porphyrin in the presence of UVA irradiation. The photocatalytic system could also be applied for the efficient degradation of a wide range of persistent, refractory and hazardous pollutants, as a pre/post-treatment sequence during the water remediation procedures. Performant multifunctional photoactive materials can thus be obtained, by combining materials inspired from nature with non-hazardous magnetic nanoparticles. Such sensitized photocatalysts possess attractive features and advantages which make them extremely valuable candidates for the field of

photocatalysis. Therefore, the photo-oxidation of persistent micro-pollutants using eco-friendly reusable photocatalysts has a great potential to become an essential treatment sequence as part of the modern green technology for water clean-up.

Acknowledgments

The authors thank BAM for the guest scientist grant of Dr. M. Neamtu. The authors acknowledge the contributions and thank to Dr. G. Ababei (HR-TEM measurements), Eng. M. Porcescu (XRD analyses), Dr. M. Grigoras (VSM measurements), Dr. M. Gaburici (FTIR recordings) from National Institute of Research and Development for Technical Physics in Iasi, Romania and to Mrs. S. Benemann (SEM/EDX measurements) and Dr. A. Paul (ESR facilities) from BAM.

Appendix A. Supplementary data

Supplementary material related to this article can be found, in the online version, at doi:<https://doi.org/10.1016/j.apcatb.2018.03.079>.

References

- W.V. Atul, G.S. Gaikwad, M.G. Dhone, N.T. Khaty, S.R. Thakare, Removal of organic pollutant from water by heterogenous photocatalysis: a review, *Res. J. Chem. Environ.* 17 (2013) 84–94.
- Y.L. Pang, S. Lim, H.C. Ong, W.T. Chong, Research progress on iron oxide-based magnetic materials: Synthesis techniques and photocatalytic applications, *Ceram. Int.* 42 (2016) 9–34.
- G. Mamba, A. Mishra, Advances in magnetically separable photocatalysts: smart, recyclable materials for water pollution mitigation, *Catalysts* 6 (2016) 79.
- I. Gultekin, N.H. Ince, Synthetic endocrine disruptors in the environment and water remediation by advanced oxidation processes, *J. Environ. Manage.* 85 (2007) 816–832.
- K. Sridharan, *Emerging Trends of Nanotechnology in Environment and Sustainability: A Review-Based Approach*, Springer, 2018.
- A.Q. Acton, Edition, *Advances in Research and Application*, (2013) Scholarly Editions ed..
- M. Yamamoto, Y. Nishizawa, P. Chabera, F.S. Li, T. Pascher, V. Sundstrom, L.C. Sun, H. Imahori, Visible light-driven water oxidation with a subporphyrin sensitizer and a water oxidation catalyst, *Chem. Commun.* 52 (2016) 13702–13705.
- T. Hasobe, Porphyrin-based supramolecular nanoarchitectures for solar energy conversion, *J. Phys. Chem. Lett.* 4 (2013) 1771–1780.
- Y.Z. Chen, A.X. Li, Z.H. Huang, L.N. Wang, F.Y. Kang, Porphyrin-based nanostructures for photocatalytic applications, *Nano Sci. Nano Technol.: Indian J.* (2016) 6.
- M.L. Marin, L. Santos-Juanes, A. Arques, A.M. Amat, M.A. Miranda, Organic photocatalysts For the oxidation of pollutants and model compounds, *Chem. Rev.* 112 (2012) 1710–1750.
- A. Vargas, B. Pegaz, E. Debeve, Y. Konan-Kouakou, N. Lange, J.P. Ballini, H. van den Bergh, R. Gurny, F. Delie, Improved photodynamic activity of porphyrin loaded into nanoparticles: an in vivo evaluation using chick embryos, *Int. J. Pharm.* 286 (2004) 131–145.
- A. Vargas, M. Eid, M. Fanchaouy, R. Gurny, F. Delie, In vivo photodynamic activity of photosensitizer-loaded nanoparticles: Formulation properties, administration parameters and biological issues involved in PDT outcome, *Eur. J. Pharm. Biopharm.* 69 (2008) 43–53.
- A.E. Chavez-Guajardo, L. Maqueira, J.C. Medina-Llamas, J. Alcaraz-Espinoza, T.L. Araujo, G.M. Vinas, A.R. Rodrigues, K.G.B. Alves, C.P. de Melo, Use of magnetic and fluorescent polystyrene/tetraphenylporphyrin/maghemite nanocomposites for the photoinactivation of pathogenic bacteria, *React. Funct. Polym.* 96 (2015) 39–43.
- A.C. Scanone, N.S. Gsponer, M.G. Alvarez, E.N. Durantini, Photodynamic properties and photoinactivation of microorganisms mediated by 5,10,15,20-tetrakis(4-carboxyphenyl)porphyrin covalently linked to silica-coated magnetite nanoparticles, *J. Photochem. Photobiol. A Chem.* 346 (2017) 452–461.
- E. Alves, M.A.F. Faustino, M. Neves, A. Cunha, H. Nadais, A. Almeida, Potential applications of porphyrins in photodynamic inactivation beyond the medical scope, *J. Photochem. Photobiol. C-Photochem. Rev.* 22 (2015) 34–57.
- C.K. Lim, J. Heo, S. Shin, K. Jeong, Y.H. Seo, W.D. Jang, C.R. Park, S.Y. Park, S. Kim, I.C. Kwon, Nanophotosensitizers toward advanced photodynamic therapy cancer, *Cancer Lett.* 334 (2013) 176–187.
- W.W. Tu, J.P. Lei, P. Wang, H.X. Ju, Photoelectrochemistry of free-base-porphyrin-functionalized zinc oxide nanoparticles and their applications in Biosensing, *Chem.-Eur. J.* 17 (2011) 9440–9447.
- G. Magna, Y. Sivalingam, A. Babbi, E. Martinelli, R. Paolesse, C.Di Natale, Drift correction in a porphyrin-coated ZnO nanorods gas sensor, 28th European Conference on Solid-State Transducers (Eurosensors 2014) 87 (2014) 608–611.
- R. Buntent, A. Intasiri, W. Lueangchaichaweng, Facile synthesis of silica monolith doped with meso-tetra(p-carboxyphenyl)-porphyrin as a novel metal ion sensor, *J. Colloid Interface Sci.* 347 (2010) 8–14.
- J.J. Inbaraj, M.V. Vinodu, R. Gandhidasan, R. Murugesan, M. Padmanabhan, Photosensitizing properties of ionic porphyrins immobilized on functionalized solid polystyrene support, *J. Appl. Polym. Sci.* 89 (2003) 3925–3930.
- G. Huang, P. Wang, L. Shen, Y.X. Wei, K. Zeng, S.J. Wei, Porous chitosan-supported metal tetra(4-carboxyphenyl) porphyrin as a practical model for the hydrophobic pocket/cavity of cytochrome P-450 enzyme, *Mater. Sci. Eng. C-Mater. For. Biol. Appl.* 49 (2015) 844–850.
- M. Benaglia, T. Danelli, F. Fabris, D. Sperandio, G. Pozzi, Poly(ethylene glycol)-supported tetrahydroxyphenyl porphyrin: A convenient, recyclable catalyst for photooxidation reactions, *Org. Lett.* 4 (2002) 4229–4232.
- O.J. Fakayode, S.P. Songca, O.S. Oluwafemi, Singlet oxygen generation potential of thiolated methoxy-polyethyleneglycol encapsulated superparamagnetic iron oxide nanoparticles-gold core-shell meso-5, 10, 15, 20-tetrakis (4-hydroxyphenyl) porphyrin, *Mater. Lett.* 199 (2017) 37–40.
- S. Takagi, M. Eguchi, D.A. Tryk, H. Inoue, Porphyrin photochemistry in inorganic/organic hybrid materials: Clays, layered semiconductors, nanotubes, and mesoporous materials, *J. Photochem. Photobiol. C-Photochem. Rev.* 7 (2006) 104–126.
- F. Bedioui, Zeolite-encapsulated and clay-intercalated metal porphyrin, phthalocyanine and Schiff-base complexes as models for biomimetic oxidation catalysts - an overview, *Coord. Chem. Rev.* 144 (1995) 39–68.
- J. Demel, K. Lang, Layered hydroxide-porphyrin hybrid materials: synthesis, structure, and properties, *Eur. J. Inorg. Chem.* (2012) 5154–5164.
- V. Hequet, P. Le Cloirec, C. Gonzalez, B. Meunier, Photocatalytic degradation of atrazine by porphyrin and phthalocyanine complexes, *Chemom. Intell. Lab. Syst. 41* (2000) 379–386.
- V.A. Faraon, R.M. Senin, S.M. Doncea, R.M. Ion, Porphyrin - zeolite materials synthesis and their use in the photocatalytic oxidation of aromatic compounds, *J. Optoelectron. Adv. Mater.* 18 (2016) 160–164.
- W. Kim, J. Park, H.J. Jo, H.J. Kim, W. Choi, Visible light photocatalysts based on homogeneous and heterogenized tin porphyrins, *J. Phys. Chem. C* 112 (2008) 491–499.
- H.Y. Yoo, S.W. Yan, J.W. Ra, D. Jeon, B. Goh, T.Y. Kim, Y. Mackeyev, Y.Y. Ahn, H.J. Kim, L.J. Wilson, P.J.J. Alvarez, Y. Lee, W.H. Song, S.W. Hong, J. Kim, J. Lee, Tin porphyrin immobilization significantly enhances visible-light-photosensitized degradation of microcystins: mechanistic implications, *Appl. Catal. B-Environ.* 199 (2016) 33–44.
- S. Huh, S.J. Kim, Y. Kim, Porphyrinic metal-organic frameworks from custom-designed porphyrins, *Crystengcomm* 18 (2016) 345–368.
- J.A. Gonzalez-Delgado, P.M. Castro, A. Machado, F. Araujo, F. Rodrigues, B. Korsak, M. Ferreira, J.P.C. Tome, B. Sarmento, Hydrogels containing porphyrin-loaded nanoparticles for topical photodynamic applications, *Int. J. Pharm.* 510 (2016) 221–231.
- K.H. Choi, K.K. Wang, E.P. Shin, S.L. Oh, J.S. Jung, H.K. Kim, Y.R. Kim, Water-soluble magnetic nanoparticles functionalized with photosensitizer for photocatalytic application, *J. Phys. Chem. C* 115 (2011) 3212–3219.
- M. Moshari, M. Rabbani, R. Rahimi, Synthesis of TCPP-Fe3O4@S/SGO and its application for purification of water, *Res. Chem. Intermed.* 42 (2016) 5441–5455.
- M. Nowostawska, S.A. Corr, S.J. Byrne, J. Conroy, Y. Volkov, Y.K. Gun'ko, Porphyrin-magnetite nanoconjugates for biological imaging, *J. Nanobiotechnol.* (2011) 9.
- R. Rahimi, E.H. Fard, S. Saadati, M. Rabbani, Degradation of methylene blue via Co-TiO2 nano powders modified by meso-tetra(carboxyphenyl)porphyrin, *J. Sol-Gel Sci. Technol.* 62 (2012) 351–357.
- D.M. Chen, K.W. Wang, W.Z. Hong, R.L. Zong, W.Q. Yao, Y.F. Zhu, Visible light photoactivity enhancement via CuTCPP hybridized g-C3N4 nanocomposite, *Appl. Catal. B-Environ.* 166 (2015) 366–373.
- Y.Z. Chen, Z.H. Huang, M.B. Yue, F.Y. Kang, Integrating porphyrin nanoparticles into a 2D graphene matrix for free-standing nanohybrid films with enhanced visible-light photocatalytic activity, *Nanoscale* 6 (2014) 978–985.
- H. Ghafari, F. Mohammadi, R. Rahimi, E. Mohammadiyan, Synthesis and characterization of a new magnetic nanocomposite with metalloporphyrin (Co-TPyP) and sulfated tin dioxide (Fe3O4@SnO2/SO4²⁻), and investigation of its photocatalytic effects in the degradation of rhodamine B, *Rsc Adv.* 6 (2016) 83947–83953.
- T.T. Tang, H. Fan, S.Y. Ai, R.X. Han, Y.Y. Qiu, Hemoglobin (Hb) immobilized on amino-modified magnetic nanoparticles for the catalytic removal of bisphenol A, *Chemom. Intell. Lab. Syst.* 83 (2011) 255–264.
- L. Sun, Y.X. Li, M.D. Sun, H.G. Wang, S.F. Xu, C.Q. Zhang, Q.B. Yang, Porphyrin-functionalized Fe3O4@SiO2 core-shell magnetic colorimetric material for detection, adsorption and removal of Hg2+ in aqueous solution, *New J. Chem.* 35 (2011) 2697–2704.
- L. Fernandez, W. Borzecka, Z. Lin, R.J. Schneider, K. Huvaere, V.I. Esteves, A. Cunha, J.P.C. Tome, Nanomagnet-photosensitizer hybrid materials for the degradation of 17 beta-estradiol in batch and flow modes, *Dyes Pigments* 142 (2017) 535–543.
- L. Fernandez, V.I. Esteves, A. Cunha, R.J. Schneider, J.P.C. Tome, Photodegradation of organic pollutants in water by immobilized porphyrins and phthalocyanines, *J. Porphyrins Phthalocyanines* 20 (2016) 150–166.
- J.C. Barona-Castano, C.C. Carmona-Vargas, T.J. Brocksom, K.T. de Oliveira, Porphyrins as catalysts in scalable organic reactions, *Mol. Cell. Probes* (2016) 21.
- J.H. Bang, K.S. Suslick, Applications of ultrasound to the synthesis of nanostructured materials, *Adv. Mater.* 22 (2010) 1039–1059.
- F. Dang, N. Enomoto, J. Hojo, K. Enpuku, Sonochemical synthesis of monodispersed magnetite nanoparticles by using an ethanol-water mixed solvent, *Ultrason. Sonochem.* 16 (2009) 649–654.

- [47] M. Abbas, M. Takahashi, C. Kim, Facile sonochemical synthesis of high-moment magnetite (Fe₃O₄) nanocube, *J. Nanopart. Res.* 15 (2013).
- [48] C. Nadejde, M. Neamtu, V.-D. Hodoroba, R.J. Schneider, A. Paul, G. Ababei, U. Panne, Green fenton-like magnetic nanocatalysts: Synthesis, characterization and catalytic application, *Appl. Catal. B-Environ.* 176 (2015) 667–677.
- [49] C. Nadejde, M. Neamtu, V.-D. Hodoroba, R.J. Schneider, G. Ababei, U. Panne, Hybrid iron-based core-shell magnetic catalysts for fast degradation of bisphenol A in aqueous systems, *Chem. Eng. J.* 302 (2016) 587–594.
- [50] A. Mukhopadhyay, N. Joshi, K. Chattopadhyay, G. De, A facile synthesis of PEG-coated magnetite (Fe₃O₄) nanoparticles and their prevention of the reduction of cytochrome C, *ACS Appl. Mater. & Interfaces* 4 (2012) 142–149.
- [51] G.Q. Lin, H.M. Ding, R.F. Chen, Z.K. Peng, B.S. Wang, C. Wang, 3D Porphyr. based covalent org. frameworks, *J. Am. Chem. Soc.* 139 (2017) 8705–8709.
- [52] H.G. Jeong, M.S. Choi, Design and properties of porphyrin-based singlet oxygen generator, *Isr. J. Chem.* 56 (2016) 110–118.
- [53] A.N. Meng, L.X. Chaihu, H.H. Chen, Z.Y. Gu, Ultrahigh adsorption and singlet-oxygen mediated degradation for efficient synergetic removal of bisphenol A by a stable zirconium-porphyrin metal-organic framework, *Sci. Rep.* 7 (2017) 9.
- [54] R. Gerdes, D. Wohrle, W. Spiller, G. Schneider, G. Schnurpfeil, G. Schulz-Ekloff, Photo-oxidation of phenol and monochlorophenols in oxygen-saturated aqueous solutions by different photosensitizers, *J. Photochem. Photobiol. A Chem.* 111 (1997) 65–74.
- [55] P. Alonso-Cristobal, M.A. Lopez-Quintela, R. Contreras-Caceres, E. Lopez-Cabarcos, J. Rubio-Retama, M. Laurenti, Synthesis of catalytically active gold clusters on the surface of Fe₃O₄@SiO₂ nanoparticles, *Rsc Adv.* 6 (2016) 100614–100622.
- [56] G.P. Yao, J. Li, Y. Luo, W.J. Sun, Efficient visible photodegradation of 4-nitrophenol in the presence of H₂O₂ by using a new copper(II) porphyrin-TiO₂ photocatalyst, *J. Mol. Catal. A Chem.* 361 (2012) 29–35.
- [57] M. Neamtu, F.H. Frimmel, Degradation of endocrine disrupting bisphenol A by 254 nm irradiation in different water matrices and effect on yeast cells, *Water Res.* 40 (2006) 3745–3750.
- [58] H. Katsumata, S. Kawabe, S. Kaneco, T. Suzuki, K. Ohta, Degradation of bisphenol A in water by the photo-fenton reaction, *J. Photochem. Photobiol. A Chem.* 162 (2004) 297–305.
- [59] C. Li, X.Z. Li, N. Graham, N.Y. Gao, The aqueous degradation of bisphenol A and steroid estrogens by ferrate, *Water Res.* 42 (2008) 109–120.
- [60] T. Olmez-Hanci, D. Dursun, E. Aydin, I. Arslan-Alaton, B. Girit, L. Mita, N. Diano, D.G. Mita, M. Guida, S₂O₈²⁻/UV-C and H₂O₂/UV-C treatment of bisphenol A: assessment of toxicity, estrogenic activity, degradation products and results in real water, *Chemom. Intell. Lab. Syst.* 119 (2015) S115–S123.